Deep three-photon functional imaging in the mouse cortex with adaptive optics

Huriye Atilgan[1]*, Jingyu Wang[2]*, Qi Hu[2]*,
Sandra Tan[1], Blake Russell[1], Martin J. Booth[2+], Armin Lak[1+]

*[+]These authors contributed equally to this work

[1]Department of Physiology, Anatomy, and Genetics, University of Oxford, Oxford, UK

[2]Department of Engineering Science, University of Oxford, Oxford, UK

Corresponding author: huriye.atilgan@dpag.ac.ox.uk

Abstract

Three-photon (3P) microscopy enables functional imaging at greater depths in the mammalian brain than any other technique with single-cell resolution, owing to greater penetration ability. One of the main challenges of such imaging is tissue-induced optical aberration, which inevitably reduces the excitation confinement at depth. Adaptive optics systems, by using deformable mirrors or other wavefront-shaping devices to compensate for optical distortions, enable real-time correction of these aberrations. In this study, we present a practical adaptive optics-assisted 3P imaging system optimized for in vivo functional recordings in the mouse cortex during behaviour. We introduce a hierarchical, three-level aberration correction strategy that sequentially targets aberration caused by the microscope system, the cranial window, and tissue depth. We demonstrate the application of this aberration correction strategy in two anatomically distinct regions—the prelimbic cortex, adjacent to the superior sagittal sinus, and the somatosensory cortex as a representative lateral cortical area—highlighting how aberration sources vary with imaging geometry. Adaptive optics significantly improved imaging performance in both contexts: restoring cellular visibility adjacent to large vascular structures in the prelimbic cortex, and enhancing signal-to-noise ratio during deep imaging in the lateral somatosensory cortex. Together, our work provides a practical framework for implementing adaptive optics-assisted 3P imaging and optimizing deep in vivo functional imaging performance across diverse cortical environments.

Introduction

Recent advances in three-photon (3P) microscopy have demonstrated its potential for studying deep tissue neuronal activity underlying behavior (Horton et al., 2013; Ouzounov et

al., 2017; Wang & Xu, 2020; Xiao et al., 2023). However, imaging at such depths presents substantial technical challenges due to the complex and heterogeneous optical environment of the brain. As light penetrates deeper into tissue, it undergoes scattering and absorption, while also encountering wavefront distortions introduced by system misalignments and sample refractive index mismatches. While all care has been taken during system building and sample preparation to reduce misalignments, tiny tilts of the cranial window, the slight off-axis positions and tilts of optics (such as relay lenses, scanning mirrors, dichroic mirrors, and the objective lens), and inhomogeneities in the tissue itself can introduce wavefront distortions (or equivalently phase aberrations). These aberrations degrade the point spread function and reduce the signal-to-noise ratio (SNR), ultimately limiting spatial resolution and image quality at depth.

Adaptive optics (AO) offers a promising solution by actively correcting aberrations. Originally developed for astronomy, AO subsystems use deformable mirrors or other wavefront-shaping devices to compensate for optical distortions, allowing the imaging beam to maintain a tight focus deep within the tissue. In doing so, AO significantly improves image sharpness, contrast, and signal strength, thereby enabling high-resolution functional imaging even in challenging, optically heterogeneous environments.

In this paper, we provide a practical methodology of an AO-assisted 3P imaging system optimised for functional in vivo recordings. We introduce a streamlined protocol for correcting optical microscope system-, cranial window-, and tissue-induced aberrations, enabling high-resolution functional imaging of neuronal dynamics at different depths and locations in the mouse cortex.

Deep imaging in the mammalian brain is fundamentally constrained by light scattering, absorption, and optical aberrations introduced by biological tissues. 3P microscopy has emerged as a powerful technique for functional imaging at greater depths, owing to its use of longer excitation wavelengths and reduced scattering (Takasaki et al., 2019). However, as imaging depth increases, optical distortions from both the microscope system and the tissue, along with reduced light intensity due to absorption, make it harder to maintain a sharp focus, resulting in lower image resolution and weaker signals (Ji et al., 2012). While system-induced aberrations from misalignment can often be corrected with a static compensator, sample-induced aberrations are more complex—they vary with imaging depth, brain region, individual samples, and even with surgical or mounting procedures. As a result, precise wavefront correction directly at the imaging plane is essential, making AO a key technology for preserving resolution and signal quality during deep imaging. (Booth, 2014; Hampson et al., 2021; Sinefeld et al., 2022; Streich et al., 2021; Xiaodong Tao et al., 2017).

AO systems typically consist of a wavefront corrector, such as a deformable mirror, to modulate the wavefront, and relay optics to direct the precompensated beam toward the sample. To measure the optical aberrations required for precompensation, both direct wavefront sensing and indirect image-based wavefront correction methods can be adopted (Kristin N. Walker & Robert K. Tyson, 2009; Turaga & Holy, 2010; Wahl et al., 2019). The indirect wavefront correction method is advantageous because of its simplicity. It is often performed using aberration modes such as Zernike polynomials (Zernike, 1934), a set of orthogonal polynomials that represent distinct types of wavefront distortions. These modes assemble commonly known classic microscopic aberrations such as coma, astigmatism, and

trefoil. All these aberrations lead to image blurring in the lateral plane and spherical aberrations, which elongate the excitation focus in the axial direction, often manifesting as weakening signal, blurring, and reduced axial resolution.

To guide effective implementation, we first introduce a hierarchical, three-level aberration correction strategy, targeting system-induced, cranial window-related, and deep tissue-specific distortions. We then demonstrate the necessity and application of this approach in two distinct imaging contexts: lateral cortical regions and regions proximal to the superior sagittal sinus. These use cases illustrate how the adaptive optics system can be flexibly tuned depending on anatomical constraints and beam path geometry to achieve optimal imaging performance, showcasing the utility of AO in enhancing 3P imaging.

Results

Enhanced functional deep imaging with adaptive optics

In this study, we presented a practical and robust three-photon (3P) imaging system optimized for in vivo recordings during a Pavlovian conditioning task in head-fixed mice. Our system utilized a Chronus femtosecond 3P laser unit (Light Conversion), integrating the pump laser, optical parametric amplifier, and prism compressor into a compact and efficient configuration. This setup delivered a stable 1300 nm beam, ideal for deep-tissue imaging applications. To further enhance image quality and correct optical aberrations, we incorporated a custom adaptive optics (AO) system. The beam was first expanded using a telescope before passing through a deformable mirror, with relay optics that conjugated the DM to the back pupil plane of the objective lens.

Beyond the AO system, the remainder of the imaging pipeline followed a conventional laser-scanning multiphoton microscope design. A pair of galvanometric scanners operating at 4 Hz was used for 256 × 256-pixel imaging, which was suitable for the lower repetition rates of 3P lasers. Fluorescence signals were collected with two photomultiplier tubes (PMTs) separated by a dichroic filter cutting at 565 nm and coupled to a 16×, 0.8 NA Nikon objective lens (**Figure 1A**; see Methods for details), which provided sufficient numerical aperture for imaging depths of up to ~950 µm.

To demonstrate the system's performance, we trained mice in a Pavlovian conditioning task in which an auditory stimulus (1.5 seconds) was followed by a liquid reward on 80 % of trials. For recordings, we targeted the prelimbic cortex—a region implicated in reward valuation and decision-making processes in rodents (Diehl & Redish, 2023; Lak et al., 2020; McLaughlin et al., 2021; Palmer et al., 2024; Sul et al., 2010; Zeeb et al., 2015). Cranial windows were implanted over the prelimbic cortex, located near the sagittal sinus and approximately 1.9 mm anterior to bregma. Imaging was conducted at 800–900 µm depths while the mice performed the Pavlovian task. The field of view (FOV) for each recording was optimized using the AO protocol outlined below

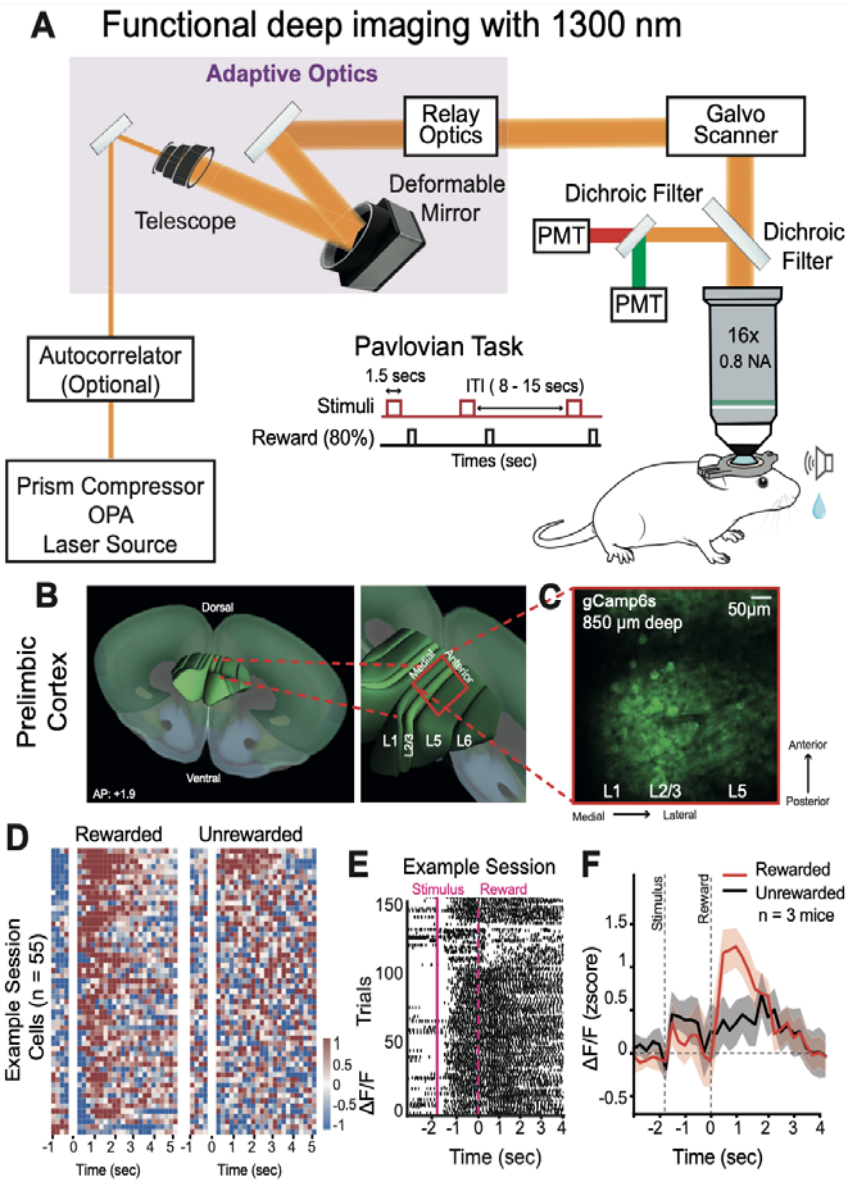

Figure 1: Functional deep imaging with 1300 nm for in vivo recordings from the prelimbic cortex during behavioral performance in mice

(A) Schematic of the 3P imaging system, which includes adaptive optics for aberration correction, a telescope and deformable mirror for beam shaping, and relay optics. The laser unit (Chronus femtosecond 3P) delivers 1300 nm light, which is directed through a galvo scanner and dichroic filters to two PMTs. A 16x, 0.8 NA Nikon objective lens is used for deep tissue imaging. **(B)** 3D model showing the placement of the cranial window over the prelimbic cortex in the mouse brain (AP = +1.9), with a zoomed-in view highlighting cortical layers L1, L2/3, L5, and L6. **(C)** In vivo image from the prelimbic cortex at a depth of 850 µm, showing gCaMP6s expression in layers L1, L2/3, L5, and L6. **(D)** Example session traces from rewarded (left) and unrewarded (right) trials, showing the change in fluorescence (ΔF/F) across cells (n = 55) recorded in the prelimbic cortex. The reward-aligned heatmap illustrates the temporal dynamics of neural activity during the auditory Pavlovian task. **(E)** Example lick raster for an example session (n = 150 trials). Each row is one trial; dots mark individual licks (stimulus onset; solid magenta line at -1.5 second and reward delivery; dashed magenta line at 0 second) Anticipatory licks before reward reflect learned stimulus–reward associations. **(F)** Average neural responses to rewarded (red) and unrewarded (black) trials across 3 mice (n = 6 sessions, 2 sessions per mouse; 329 cells). Z-scored ΔF/F values are plotted over time, showing significant differences in neural activity during the stimulus and reward periods, demonstrating the system's ability to capture decision-making processes in vivo.

Despite cell-type-specific labeling of excitatory neurons with CamKIIα promoter-driven GCaMP6s expression, we observed notable somatic size variability within our FOVs (**Figure 1C**). This variability primarily arises because in the prelimbic areas, cortical layers are perpendicular to the imaging plane. Therefore, imaging fields encompass neurons across multiple cortical layers within a single imaging plane (**Figure 1B and 1C**), each containing distinct pyramidal neuron subtypes and characteristic soma sizes (Benavides-Piccione et al., 2006; Gerfen et al., 2018; Harris & Shepherd, 2015; Molnár & Cheung, 2006). While optical aberrations at depth may also contribute to apparent size differences, the dominant source of variability in our recordings is the biological diversity across layers, spanning from superficial to deep layers within a single FOV.

The scanning speed was set to 4 Hz due to the low repetition rate of the light source required for three-photon imaging; this rate was sufficient to capture task-related neural dynamics during the Pavlovian conditioning. For cell detection, we used Suite2p (Pachitariu et al., 2016), followed by manual curation (see Methods). However, because of the considerable variation in cell size across layers, automatic detection alone proved insufficient. We therefore combined the Suite2p output with manual curation to ensure accurate identification of somatic masks. Using this approach, we identified 329 cells across six sessions from three mice (mean = 55 cells/session, SD = 31; max = 119; min = 23). Example session heatmaps showed distinct patterns of activity for rewarded versus unrewarded trials (**Figure 1D**), and population-averaged neural responses demonstrated clear responses to stimulus onset as well as outcome-dependent differences at reward delivery (**Figure 1E**). These results demonstrated that our adaptive-optics–enhanced three-photon system can reliably resolve both stimulus- and outcome-related neural activity in deep cortical layers. While our recordings reveal rich neural dynamics during the decision-making task, a detailed interpretation of how these dynamics vary across layers is beyond the scope of the present study.

Multi-level aberration compensation required for optimal imaging in mice

In optimizing our system for deep imaging, we developed a novel, hierarchical aberration correction protocol tailored for in vivo three-photon imaging in the mouse brain (Table 1, **Figure 2A**). This approach systematically targets aberrations introduced at different stages of the experimental setup, resulting in improved image quality and signal fidelity across imaging depths.

<u>1. System-level aberration correction</u>

We first addressed system-induced aberrations—such as coma, astigmatism, and spherical aberrations—by imaging a fixed slide containing fluorescent beads (diameter 500 nm) under a cranial window mounted in place. These types of aberrations are common in most setups, with coma and astigmatism arising from optical misalignments and spherical aberrations primarily caused by the presence of the cranial window or lack of a correction collar on the objective lens. Using this preparation, we optimized the adaptive optics (AO) system to generate a baseline correction, referred to as the "system flat," that is different from a flat deformable mirror that is commonly called DM flat. This correction is applied uniformly across all animals imaged with the same optical setup and serves as the foundation for all

subsequent adjustments. At this stage, we corrected for 22 Zernike modes. Although optimizing a large number of modes is time-consuming (with 3-5 measurements per mode to estimate the desired correction on the deformable mirror, see methods for details), this procedure is performed only once, and the resulting correction is saved for future use.

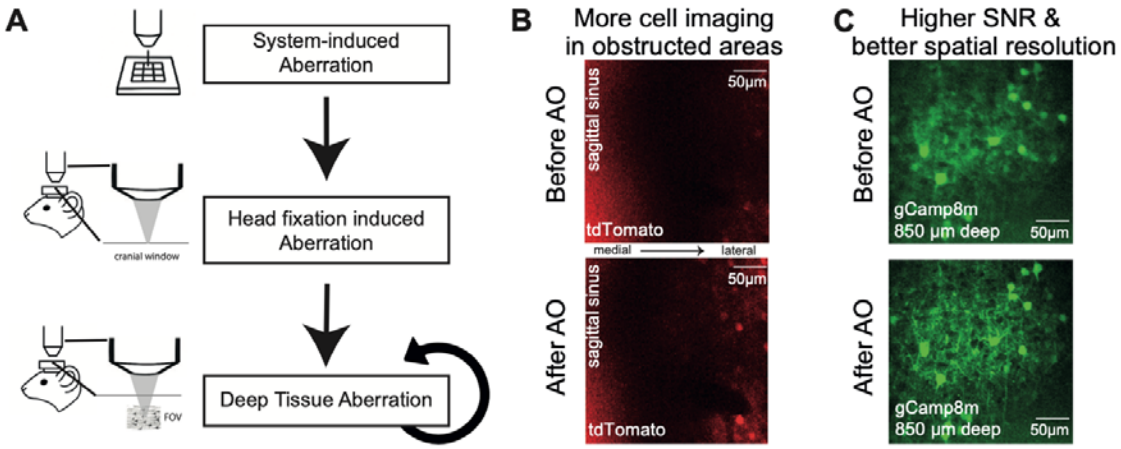

Figure 2: Multi-level aberration correction improves deep tissue imaging performance
(A) Schematic overview of the hierarchical aberration correction protocol. Aberrations were sequentially corrected at three stages: system-induced aberrations, head-fixation-induced aberrations, and deep tissue aberrations. **(B)** Representative in vivo tdTomato images near the sagittal sinus region before (top) and after (bottom) adaptive optics (AO) correction. Use of red emission detection at 1300 nm excitation enhanced visualization of cortical static labelled cells, enabling improved imaging even in highly obstructed regions. **(C)** Representative in vivo GCaMP8m images at ~850 µm depth before (top) and after (bottom) full AO correction. AO correction substantially improved signal-to-noise ratio (SNR) and spatial resolution.

2. Head-fixation-induced aberration correction

Next, we corrected for aberrations introduced by slight variations in cranial window alignment during head fixation. After applying the system flat, we imaged a superficial cortical plane to identify and correct residual astigmatism and coma. Although our functional indicator (GCaMP6s and GCaMP8s) fluoresced in the green channel, surface cortical fibers exhibited strong autofluorescence in the red channel—providing a stable structural reference that did not fluctuate with neural activity. Static labeling is inherently more reliable for adaptive-optics correction because it yields a constant signal against which aberrations can be measured. In principle, either channel could serve for alignment, but in our setup, the red autofluorescence made surface fibers readily visible, so we captured red emission with a red-filtered PMT at 1,300 nm excitation to efficiently detect and correct residual aberrations.

This approach allowed us to efficiently visualize and adjust for superficial distortions before proceeding to deeper imaging. The same correction also improves the image from the green channel effectively, as the system and head fixation-induced aberrations are mostly achromatic. Head-fixation correction was performed once per animal and ensured that inter-

animal variability in head positioning did not propagate to deeper imaging layers. Head-fixation error usually leads to a small misalignment of the cranial window that introduces comas; slight differences in the thickness of the glass could introduce spherical aberrations. To minimize preparation time, we limited this correction step to four modes: two astigmatisms and two comas, with 5 aberration biases per mode.

3. Deep tissue aberration correction

Finally, we addressed the complex and heterogeneous aberrations arising from light scattering and refractive index mismatches in deep brain tissue. These include higher-order distortions such as trefoil and secondary spherical aberrations. Following the first two correction steps, we targeted the region of interest (ROI) and applied iterative AO optimization to achieve localised correction.

To optimize this deep tissue correction, it is straightforward to use the imaging channel (usually green) to provide aberration information; we commonly conveniently employed static red fluorescent labeling within the ROI to guide the sensorless adaptive optics approach. The presence of a stable, non-activity-dependent signal was critical for accurately measuring and refining the wavefront during iterative optimization. While GCaMP6s activity-dependent signals were available, static red labeling provided a more reliable and stable reference for correction, as green signals fluctuated with spontaneous and evoked neural activity. The use of static red fluorescence substantially improved the accuracy and efficiency of deep tissue AO correction, enabling restoration of high-resolution imaging at depth across variable cortical environments.

Table 1: Aberration correction protocol for deep tissue imaging

Aberration Source	Possible Aberrations	Frequency	Protocol
1. System-induced aberration	Coma, astigmatism, spherical	Once per imaging system	Use a fixed calibration slide. Position a cranial window used on the mice on a slide and get the best wavefront correction (called '*system flat*'). Apply these values to all recordings as default starting parameters.
2. Head fixation-induced aberration	Coma, spherical	Once per animal	After applying the system flat, image a superficial layer of positioned mice and correct for residual coma and tilt introduced by head fixation.
3. Deep tissue aberration	All aberration modes, mainly coma, trefoil, astigmatism, spherical, and secondary levels	Once per region of interest (ROI)	After correcting system and head fixation aberrations, locate your ROI. Run a few correction iterations to optimize the wavefront shape at depth. First, using large steps, then using the fine steps.

This three-tier correction protocol enhanced the cell visibility (**Figure 2B**) as well as improved imaging contrast, signal-to-noise ratio, and spatial resolution (**Figure 2C**), particularly in deep cortical layers. By isolating and compensating for aberrations at each source — system, head fixation, and tissue — we demonstrate that a sequential, targeted approach to aberration correction yields good imaging performance.

Application of Aberration Correction Across Distinct Anatomical Contexts

To further evaluate the robustness of our correction strategy, we applied the protocol in two anatomically distinct recording contexts: the prelimbic cortex which its proximity to superior sagittal sinus causes difficulty in imaging **(Figure 3)** and the lateral somatosensory cortex, where imaging could be challenging due to lateral position of FOV (**Figure 4**).

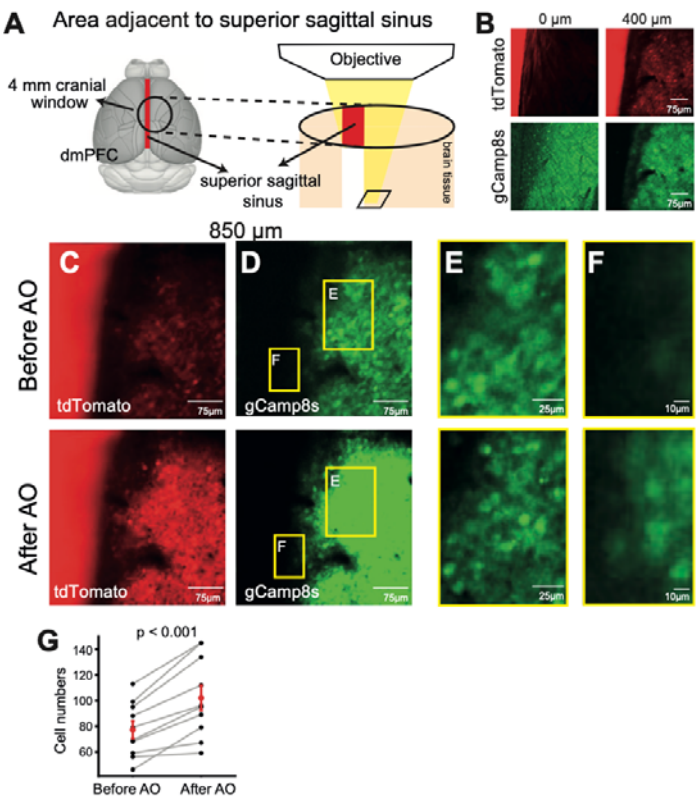

Figure 3: Adaptive optics improves cellular visibility and signal quality near the superior sagittal sinus

(A) Schematic showing imaging fields positioned adjacent to the superior sagittal sinus in the anterior cingulate cortex ACC) through a 4 mm cranial window. **(B)** tdTomato (top) and GCaMP8s (bottom) fluorescence images at the cortical surface (0 µm) and at 400 µm depth, illustrating the optical challenges imposed by the sinus region. **(C–D)** Representative tdTomato (C) and GCaMP8m **(D)** images at ~850 µm depth before (top) and after (bottom) adaptive optics (AO) correction. The same contrast settings were applied to the before and after images to allow direct visual comparison of signal improvement. **(E–F)** Magnified views of example subregions (E and F, indicated in yellow boxes in D) showing finer somatic structures before and after AO correction. Their contrast is optimised for each image. **(G)** Quantification of detected cell numbers before and after AO correction from three different mice (each data point represents one field of view). Cell detection was performed using Suite2p output combined with manual curation. Rigid motion correction (Suite2p) was applied to all recordings prior to analysis. Imaging was performed at 256 × 256 pixel resolution, 4 Hz frame rate, with 1-minute recordings averaged over 240 frames. Statistical comparison by paired t-test, $p < 0.001$.

In the medial prelimbic cortex, imaging fields were positioned close to the midline, where the superior sagittal sinus creates both anatomical and optical challenges at the cortical surface (**Figure 3A**). The sinus, a large blood-filled vessel, introduces significant refractive index heterogeneity and physical obstruction along the excitation path, complicating efforts to image deeper cortical regions (e.g., ~800 µm below the surface). In these areas, a part of the excitation beam must pass through the sinus, often resulting in substantial signal loss, beam distortion, or complete blockage. This anatomical constraint can severely limit access to otherwise viable ROIs. Depth-resolved imaging before correction revealed pronounced signal degradation and image distortion beginning as early as 300–500 µm depth (**Figure 3B**). Following full aberration correction, we observed marked improvements in cell visibility across depths up to 850µm (**Figure 3C**), even in areas adjacent to the sinus (**Figure 3F**).

Adaptive optics compensated for the wavefront distortions introduced by the complex optical environment near the superior sagittal sinus. This region presents a particularly challenging imaging context due to refractive index mismatches not only from the cranial window and the immersion medium, but also from brain tissue ($n \approx 1.36–1.37$) and blood ($n \approx 1.35–1.39$, depending on oxygenation and hematocrit). These mismatches cause localized phase delays, wavefront aberrations, and focal curvature across the imaging plane, leading to rapid degradation of spatial resolution and contrast, even at relatively shallow depths. By correcting low-order aberrations (e.g., coma, astigmatism, spherical aberration, trefoil) based on the unique optical features of each imaging FOV, AO restoration enabled finer somatic structures to re-emerge with high clarity and signal fidelity, significantly enhancing cell visibility even in regions adjacent to major vasculature. Although the absorption caused by the tissue cannot be recovered, the benefits of AO correction were consistently replicable across different ROIs within individual mice and across multiple mice, as quantified by improved signal fidelity in 10 ROIs from 3 mice (paired t-test, $t_{19} = 3.567$, $p < 0.001$; **Figure 3G**).

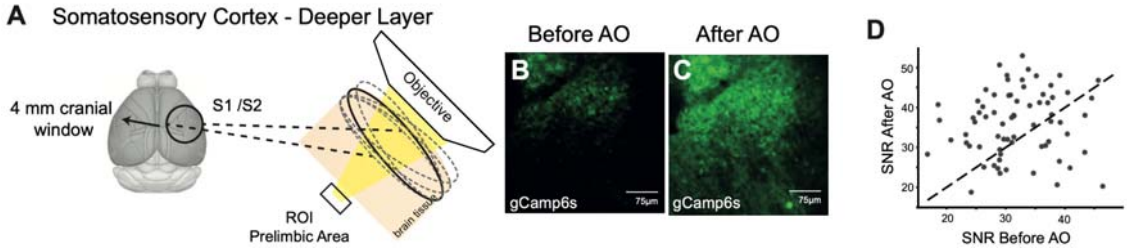

Figure 4: Adaptive optics improves signal-to-noise ratio during deep imaging in the lateral somatosensory cortex

(A) Schematic showing the imaging strategy targeting deep layers (~800–900 µm) of the lateral somatosensory cortex (S2) through a 4 mm cranial window. **(B–C)** Representative GCaMP6s images at ~850 µm depth before (B) and after (C) adaptive optics (AO) correction. The same contrast settings were applied to both images to allow direct comparison of signal enhancement following correction. **(D)** Quantification of signal-to-noise ratio (SNR) improvements for individual cells before and after AO correction. Each dot represents one cell (n = 68 cells, Suite2p ROI with manual curation); SNR was calculated from mean fluorescence over time divided by standard deviation across frames for each ROI. Rigid motion correction (Suite2p) was applied to all recordings prior to analysis. Imaging was performed at 256 × 256 pixel resolution, 4 Hz frame rate, with 1-minute recordings averaged over 240 frames.

We next applied our multi-level aberration correction strategy to recordings in the lateral somatosensory cortex, a representative example of more lateral cortical areas (**Figure 4A**). In contrast to imaging near the midline, the lateral cortex presented a more uniform surface morphology, with relatively fewer large surface vessels and minimal gross tissue curvature. However, imaging at depths of 800–900 μm still exhibited noticeable degradation in spatial resolution and signal intensity prior to aberration correction (**Figure 4B**). These degradations were primarily driven by deep tissue scattering and slight cranial window tilts introduced during surgical preparation, where the window was not perfectly perpendicular to the optical axis of the objective, as is often unavoidable.

Application of the full correction protocol significantly enhanced imaging quality, as evidenced by improved signal-to-noise ratio (**Figure 4D,** pairwise t-test $p = 0.024$). While the total number of visually detectable somata remained similar before and after correction (**Figure 4B-C**), AO substantially improved the clarity, contrast, and reliability of individual cell signals. This suggests that, even in lateral cortical regions without major superficial vascular structures, multi-level aberration correction is essential for maximizing functional imaging fidelity at depth.

Discussion

Our results demonstrate that integrating adaptive optics (AO) with three-photon (3P) microscopy significantly enhances deep-brain functional imaging capabilities. By systematically correcting optical aberrations at the system, cranial window, and tissue levels, we were able to extend functional imaging depths while preserving high spatiotemporal resolution. This simplified correction strategy allowed us to reliably record neuronal activity during stimulus-guided behaviour from brain regions that were previously inaccessible or severely degraded by optical distortions.

We show that the anatomical context strongly influences the distribution of aberrations encountered during deep imaging. In the medial prelimbic cortex, close to the superior sagittal sinus, large surface blood vessels introduce complex wavefront distortions through refractive index heterogeneity, leading to rapid signal degradation even at shallow depths. In contrast, in the lateral somatosensory cortex, although superficial morphology was more regular, subtle cranial window tilts and cumulative deep tissue still substantially compromised image quality at depth. AO correction markedly improved imaging performance in both contexts: restoring cellular visibility adjacent to vasculature in the prelimbic cortex and enhancing signal-to-noise ratios in the lateral cortex, even though the number of detectable cells remained constant in the latter.

Our data also highlight an important biological consideration: deep cortical layers exhibit greater morphological heterogeneity in cell size compared to superficial layers, reflecting diverse pyramidal subtypes and dendritic architectures. Because automated ROI detection algorithms can be biased by soma size, this variability poses a potential confound for both detection efficiency and downstream population-level analyses. Even in the face of such heterogeneity, AO remains critical by restoring diffraction-limited resolution. AO helps to delineate true cell boundaries across varied soma sizes. Recognizing and accounting for cell-size heterogeneity will therefore be essential in future three-photon functional imaging

studies of deep cortical circuits, ensuring that observed activity patterns truly reflect neural dynamics rather than detection artifacts.

We demonstrated that correcting low-order Zernike aberrations (coma, astigmatism, spherical aberration, trefoil) already delivers substantial gains in image quality and scientific insight for deep-tissue three-photon imaging. Looking ahead, extending this framework to higher-order modes—especially with deformable mirrors offering greater actuator density—could further counteract scattering-induced distortions and unlock even finer resolution at depth. Likewise, adopting automated optimization strategies, such as machine-learning–based AO (Hu et al., 2023), would accelerate aberration correction and dynamically adapt to complex wavefront errors. Although we chose a conventional sensorless approach here to preserve simplicity and retain precise control over individual aberration components, our protocol is fully compatible with these advanced methods—paving the way for more efficient, robust, and high-fidelity deep-tissue imaging in future studies.

In this work, we, like most AO microscopy approaches, applied a single correction pattern across each field of view—a choice that delivers clear benefits in simplicity and overall image quality, as demonstrated by our deep-tissue results. When optical aberrations vary substantially within the FOV, for example, around small blood vessels or local scattering centers, region-specific corrections may yield even higher fidelity. Future implementations could reduce the corrected FOV and synchronize the DM with the scanners for sub-region tuning, or incorporate multi-conjugate AO and direct wavefront-sensing techniques. By moving toward spatially adaptive AO strategies (Simmonds & Booth, 2013), researchers will be able to preserve the advantages of our current framework while achieving optimal aberration compensation across large, heterogeneous brain regions.

Overall, our findings emphasize that adaptive optics is a transformative tool for deep in vivo imaging, enabling high-quality functional recordings across anatomically diverse and optically challenging brain regions. With further hardware and software innovations, particularly around expanded correction modes and better depth-adaptive control, AO-assisted 3P microscopy holds substantial potential to push the boundaries of functional neuroimaging deeper into the intact brain.

Methods

Animals

All experimental procedures involving animals were conducted in accordance with the UK animals in Scientific Procedures Act (1986). Adult mice of both sexes (2-6 months of age) on a C57BL/6 background were used for experiments. We used seven transgenic mice on a CamKIIα–tTa (AI94) × B6;DBA-Tg(tetO-GCaMP) background—two expressing GCaMP8s and five expressing GCaMP6s. All mice were housed at room temperature (20–22 °C) on a standard light/dark cycle and humidity of ~40%, and provided with a standard mouse chow diet and received daily husbandry.

Surgical Procedures

Three different surgical procedures were used in this project: (1) implantation of a temporal window over the sinus, (2) implantation of a temporal window over the sinus combined with a

cranial injection of red bead in the dorsomedial striatum (DMS) leading to expression of red beads in the cortex, and (3) implantation of a lateral temporal window over the right somatosensory cortex.

All animals underwent the same anaesthetic protocol. Anaesthesia was induced with 3% isoflurane and maintained at or below 1.5% throughout surgery. Perioperative analgesia included subcutaneous administration of buprenorphine (0.1 mg/kg, Vetergesic) and meloxicam (5 mg/kg, Metacam). Additionally, bupivacaine (2 mg/kg, Marcaine) was applied topically to the scalp prior to sterilisation with chlorhexidine gluconate and isopropyl alcohol (ChloraPrep). The scalp was then bilaterally removed. The exposed skull was cleaned with a bone scraper (Fine Science Tools) to remove the periosteum. An aluminium head-plate with a 7 mm imaging well was secured to the skull using dental cement (Super-Bond C&B, Sun-Medical).

Depending on the experimental condition, mice underwent a circular craniotomy (4 mm diameter over right somatosensory cortex: –1.4 mm posterior, +4.0 mm lateral; or 4-5 mm diameter over the sagittal sinus targeting prelimbic cortex: +1.5 mm anterior, centered over the sinus) performed with a dental drill (NSK UK Ltd.). The skull within the craniotomy site was soaked with saline before removal. Bleeding, if present, was flushed with saline for at least 5 minutes before performing a durotomy.

In animals undergoing viral labelling, a single 500 nL viral injection was performed using a calibrated, sharpened glass pipette. To label DMS-projecting neurons in the prelimbic cortex, a retrograde virus expressing red fluorescent protein (rAAV2-CAG-tdTomato, 2.3×10^{13} gc/mL, 500 nL, Addgene #59462-AAVrg) was injected into the DMS (AP +0.74, ML +1.25, DV 1.8). Injections were delivered at a rate of 100 nL/min using an automated nanoinjector (Nanoject II™, Drummond). Following the injection, the pipette was left in place for 10 minutes to promote viral diffusion.

After the injection, a double-layered cranial window—composed of a 4 mm coverslip glued to a 3 mm coverslip (or a 5 mm glued to a 4 mm coverslip)—was gently pressed into the craniotomy and sealed with cyanoacrylate (VetBond) and dental cement. Mice were placed in a heated recovery chamber and monitored until fully ambulatory. Postoperative care included daily health monitoring and weight recording for 7 days.

Mice were allowed a minimum of 21 days recovery with ad libitum access to food and water prior to any further procedures, allowing sufficient time for viral expression before the onset of behavioural training.

Behavioural training

Pavlovian conditioning was employed as the training task to familiarize the auditory cue to the mice, utilizing a 1.5-second tone followed by a water reward delivered in 80% of the trials. Over a 3-5 day training period, animals were subjected to 150 trials per day, with each trial separated by an inter-trial interval (ITI) ranging from 8 to 15 seconds.

Three-photon imaging

The three-photon fluorescence microscope utilised an integrated Chronus 3P Unit (Light Conversion), which combines a wavelength-tunable optical parametric amplifier (OPA) and a

prism compressor, pumped by a femtosecond laser (1030 nm). The system operated at 1300 nm and achieved a pulse width of 49 fs under the objective lens. The laser repetition rate was maintained at 1 MHz with a maximum power of 100 mW under the objective lens. The images were acquired with a galvo scanning multiphoton microscope (VivoScope, Scientifica UK) and a water immersion objective (Nikon, 0.8 NA, 3mm working distance). We also tested a higher numerical aperture, long working distance objective (Olympus XLPLN25XSVMP2, 25×, 1.0 NA, 4 mm working distance), but observed no substantial improvement in imaging quality at these depths. Although larger NA objectives offer better transmission, theoretical benefits in resolution and collection efficiency, they are physically bulkier, making precise positioning over the cranial window more challenging. Achieving an optimal working distance often requires a larger cranial window, which in turn introduces greater susceptibility to motion artifacts. As a result, the practical complications associated with using a larger NA objective outweighed the potential optical advantages in our deep imaging experiments.

One PMT (H10770PA-40, Hamamatsu) detection channel was used to collect green fluorescence using a dichroic (T565LPXR, Chroma) and bandpass filter (ET525/50m-2p, Chroma). The second PMT detection channel was used to collect red fluorescence with a bandpass filter (ET620/60m, Chroma). The signal was then converted to voltage by a transimpedance amplifier (150 kOhm, 1 MHz; XPG-ADC-PREAMP) and sent to a channel of the digitizer of the vDAQ card (Vidrio Technologies). ScanImage 2021 (Vidrio Technologies) running on MATLAB (MathWorks) was used to acquire images. A motorized stage (Scientifica) was used to control the position of the sample, and a focusing motor (Scientifica) was used to control the position of the objective and PMT detection apparatus relative to the sample. All imaging depths are reported in raw axial movement of the motorized stage. High-resolution structural images were typically taken with 256x256 pixels per frame at 3.2 μs dwell time (4.23 Hz) and an average of 240 frames unless otherwise stated.

Adaptive Optics

An adaptive-optics Mirao 52e deformable mirror (DM) was incorporated into the excitation path. The laser beam after the OPA was first expanded to fill the DM aperture, then relayed by a telescope to conjugate the DM to the scanners and the back pupil plane of the objective lens. This pupil conjugation guarantees that wavefront corrections apply uniformly across the entire field of view in our telecentric design. To match the beam diameter to the DM's 15 mm aperture and the 3mm scanning mirrors, the expanded laser beam was reflected from the DM and passed through an 8.3x (500/60) telescope. The beam size is reduced to 1.8 mm at the scanners. After the scanners, the beam was expanded by another telescope formed by the scan lens and the tube lens to be 12.75 mm at the objective pupil plane, which underfills the objective pupil with a fill ratio of 0.85.

Before first use, the continuous-membrane DM must undergo a thorough Zernike polynomial control matrix calibration to account for individual actuator influence function. We perform this calibration on a homebuilt interferometer (design and code available at https://aomicroscopy.org/dm-calib,(Antonello et al., 2020)), where each actuator is "poked" through a range of voltages while capturing the resulting surface profiles. Custom software (https://github.com/dop-oxford/dmlib) then extracts wavefronts from the interferograms and

computes each actuator's influence function. By fitting these influence functions to a set of normalized Zernike modes, we assemble and invert a conversion matrix that maps desired Zernike polynomials to actuator voltages. This automated pipeline ensures that any prescribed wavefront correction—expressed in Zernike terms—can be delivered precisely by the DM.

During experiments, we implemented a sensorless adaptive-optics routine to correct residual aberrations without adding extra hardware or special sample preparations. Sensorless AO treats image quality metric as the feedback signal: because optimal aberration correction maximizes image intensity, sharpness, or contrast, we define an imagemetric—such as the normalized variance or high-frequency power of the fluorescence image—and then iteratively apply an intentionally biased Zernike mode on the DM to measure that metric. For each mode, we apply a set of Zernike bias, acquire an image, compute its metric value, and use a quadratic function to fit the measured curve to converge on the optimal correction. This flexible, purely image-based approach scales seamlessly across depths and sample types; for full implementation details, see Zhang et al. (2023).

In this work, we adopted a modal sensorless AO strategy, which is well-suited to our continuous□membrane DM and practical for routine use. We chose the three□photon fluorescence intensity as our image□quality metric, since improving the point□spread function directly increases three□photon yield. To ensure that metric changes reflected aberration correction rather than FOV shifts, we excluded the tip, tilt, and defocus Zernike modes—each of which translates the FOV laterally or axially—from our optimization. For each remaining aberration mode, we applied a series of known bias amplitudes and acquired images over the same fixed FOV, then computed the three□photon intensity for each bias. In the small□aberration regime (<1 rad root mean square), the metric's dependence on mode amplitude is approximately parabolic, so we fit a parabola to these data points and extracted the peak bias as the optimal correction. Because Zernike modes are orthogonal over a circular pupil, correcting one mode does not, in theory, alter the others, enabling a straightforward sequential optimization. Variations on this approach—and a discussion of its advantages and limitations—can be found in Facomprez et al. (2012).

In this paper, we used the 5N correction scheme (meaning five different known biases per mode were introduced for correction derivation). We selected two comas, two astigmatisms, two trefoils, and primary spherical as modes for correction. For each mode, the five biases are ±2 rad, ±1 rad, and 0 rad to allow an equally spaced coverage over the total range of 2 rad. Although Facomprez and his team were using a two-photon microscope for the demonstration and analysis, as pointed out in their paper, the similar concept and evaluation should be easily extended to other non-linear microscopes, such as third-harmonic generation or three-photon in our case.

Data Analysis

All data analyses were performed using custom scripts in MATLAB and Python unless otherwise noted. Image processing was intentionally kept minimal to preserve the integrity of the raw data. No spatial smoothing, sharpening, or deconvolution was applied. Images shown in figures primarily represent the average intensity projection of raw or minimally

processed frames, aiming to accurately reflect native imaging quality. Motion correction was applied using Suite2p's non-rigid motion correction algorithm (Pachitariu et al., 2016), allowing for the correction of both global and local movements across imaging frames. This step was critical to maintaining structural consistency, particularly during deep tissue imaging.

Cell numbers were determined by manually curated detection of somatic masks, initially generated using Suite2p's automated segmentation. Given the variability in soma size across cortical layers, automatic detection alone was insufficient. Automated segmentation outputs were manually reviewed and adjusted to ensure accurate identification of cells. Therefore, we combined Suite2p output with manual curation to ensure accurate identification of somatic cell masks. The total number of identified cells was then quantified for each field of view and used in comparative analyses. Statistical comparisons of cell count across conditions were also performed using two-tailed paired t-tests. Signal-to-noise ratio (SNR) was calculated by dividing the mean fluorescence intensity of the signal region, estimated from Suite2p-identified somatic masks with neuropil subtraction applied, by the standard deviation of the background signal within the same field of view. SNR comparisons across conditions were statistically evaluated using two-tailed paired t-tests.

Data and software availability

The functional three-photon calcium imaging recordings that are presented in this manuscript will be made publicly available in a GIN repository upon publication. Behavioural training used Rigbox hardware and software as previously reported (Bhagat et al., 2020). Offline pre-processing imaging analysis was performed using FIJI (Schindelin et al., 2012) and Suite2p. All subsequent data analysis and visualisation were performed in Python 3.9 using custom-written code, which will be made publicly available on Github upon publication.

Acknowledgments

We thank Prof. Randy Bruno for generously providing equipment support and for the invaluable discussions that helped guide the setup of the three-photon microscope. We are also grateful to Light Conversion, Photonics Solutions (UK) for kindly lending us the Chronus3P laser unit. This work is supported by a Sir Henry Wellcome postdoc fellowship (222807/Z/21/Z) to H. A., grants from Wellcome (213465/Z/18/Z) and UKRI (EP/X026655/1) to A.L, UKRI/Wellcome Physics of Life Grant (EP/W024047/1), European Research Council Advanced Grant (AdOMiS 695140) to M.J.B, and Schmidt Sciences LLC (Schmidt AI in Science postdoctoral research fellowship) to Q.H.

References

Antonello, J., Wang, J., He, C., Phillips, M., & Booth, M. (2020). *Interferometric calibration of a deformable mirror*. https://doi.org/10.5281/zenodo.3714951

Benavides-Piccione, R., Hamzei-Sichani, F., Ballesteros-Yáñez, I., DeFelipe, J., & Yuste, R. (2006). Dendritic Size of Pyramidal Neurons Differs among Mouse Cortical Regions. *Cerebral Cortex*, *16*(7), 990–1001. https://doi.org/10.1093/cercor/bhj041

Bhagat, J., Wells, M. J., Harris, K. D., Carandini, M., & Burgess, C. P. (2020). Rigbox: An Open-Source toolbox for probing neurons and behavior. *Eneuro*, *7*(4).

Booth, M. J. (2014). Adaptive optical microscopy: The ongoing quest for a perfect image. *Light: Science & Applications*, *3*(4), e165–e165.

Diehl, G. W., & Redish, A. D. (2023). Differential processing of decision information in subregions of rodent medial prefrontal cortex. *eLife*, *12*, e82833. https://doi.org/10.7554/eLife.82833

Facomprez, A., Beaurepaire, E., & Débarre, D. (2012). Accuracy of correction in modal sensorless adaptive optics. *Optics Express*, *20*(3), 2598–2612. https://doi.org/10.1364/OE.20.002598

Gerfen, C. R., Economo, M. N., & Chandrashekar, J. (2018). Long distance projections of cortical pyramidal neurons. *Journal of Neuroscience Research*, *96*(9), 1467–1475. https://doi.org/10.1002/jnr.23978

Hampson, K. M., Turcotte, R., Miller, D. T., Kurokawa, K., Males, J. R., Ji, N., & Booth, M. J. (2021). Adaptive optics for high-resolution imaging. *Nature Reviews Methods Primers*, *1*(1), 68.

Harris, K. D., & Shepherd, G. M. G. (2015). The neocortical circuit: Themes and variations. *Nature Neuroscience*, *18*(2), 170–181. https://doi.org/10.1038/nn.3917

Horton, N. G., Wang, K., Kobat, D., Clark, C. G., Wise, F. W., Schaffer, C. B., & Xu, C.

(2013). In vivo three-photon microscopy of subcortical structures within an intact mouse brain. *Nature Photonics*, *7*(3), 205–209. https://doi.org/10.1038/nphoton.2012.336

Hu, Q., Hailstone, M., Wang, J., Wincott, M., Stoychev, D., Atilgan, H., Gala, D., Chaiamarit, T., Parton, R. M., Antonello, J., Packer, A. M., Davis, I., & Booth, M. J. (2023). Universal adaptive optics for microscopy through embedded neural network control. *Light: Science & Applications*, *12*(1), 270. https://doi.org/10.1038/s41377-023-01297-x

Ji, N., Sato, T. R., & Betzig, E. (2012). Characterization and adaptive optical correction of aberrations during in vivo imaging in the mouse cortex. *Proceedings of the National Academy of Sciences*, *109*(1), 22–27. https://doi.org/10.1073/pnas.1109202108

Kristin N. Walker & Robert K. Tyson. (2009). *Wavefront correction using a Fourier-based image sharpness metric*. *7468*, 74680O. https://doi.org/10.1117/12.826648

Lak, A., Okun, M., Moss, M. M., Gurnani, H., Farrell, K., Wells, M. J., Reddy, C. B., Kepecs, A., Harris, K. D., & Carandini, M. (2020). Dopaminergic and Prefrontal Basis of Learning from Sensory Confidence and Reward Value. *Neuron*, *105*(4), 700-711.e6. https://doi.org/10.1016/j.neuron.2019.11.018

McLaughlin, A. E., Diehl, G. W., & Redish, A. D. (2021). Chapter Nine—Potential roles of the rodent medial prefrontal cortex in conflict resolution between multiple decision-making systems. In A. T. Brockett, L. M. Amarante, M. Laubach, & M. R. Roesch (Eds.), *International Review of Neurobiology* (Vol. 158, pp. 249–281). Academic Press. https://doi.org/10.1016/bs.irn.2020.11.009

Molnár, Z., & Cheung, A. F. P. (2006). Towards the classification of subpopulations of layer V pyramidal projection neurons. *Neuroscience Research*, *55*(2), 105–115. https://doi.org/10.1016/j.neures.2006.02.008

Ouzounov, D. G., Wang, T., Wang, M., Feng, D. D., Horton, N. G., Cruz-Hernández, J. C., Cheng, Y.-T., Reimer, J., Tolias, A. S., Nishimura, N., & Xu, C. (2017). In vivo three-photon imaging of activity of GCaMP6-labeled neurons deep in intact mouse brain.

Nature Methods, *14*(4), 388–390. https://doi.org/10.1038/nmeth.4183

Pachitariu, M., Stringer, C., Schröder, S., Dipoppa, M., Rossi, L. F., Carandini, M., & Harris, K. D. (2016). Suite2p: Beyond 10,000 neurons with standard two-photon microscopy. *BioRxiv*, 061507.

Palmer, J. A., White, S. R., Chavez Lopez, K., & Laubach, M. (2024). The Role of the Rat Prefrontal Cortex and Sex Differences in Decision-Making. *The Journal of Neuroscience*, *44*(46), e0550242024. https://doi.org/10.1523/JNEUROSCI.0550-24.2024

Schindelin, J., Arganda-Carreras, I., Frise, E., Kaynig, V., Longair, M., Pietzsch, T., Preibisch, S., Rueden, C., Saalfeld, S., & Schmid, B. (2012). Fiji: An open-source platform for biological-image analysis. *Nature Methods*, *9*(7), 676–682.

Simmonds, R. D., & Booth, M. J. (2013). Modelling of multi-conjugate adaptive optics for spatially variant aberrations in microscopy. *Journal of Optics*, *15*(9), 094010. https://doi.org/10.1088/2040-8978/15/9/094010

Sinefeld, D., Xia, F., Wang, M., Wang, T., Wu, C., Yang, X., Paudel, H. P., Ouzounov, D. G., Bifano, T. G., & Xu, C. (2022). Three-Photon Adaptive Optics for Mouse Brain Imaging. *Frontiers in Neuroscience*, *Volume 16-2022*. https://www.frontiersin.org/journals/neuroscience/articles/10.3389/fnins.2022.880859

Streich, L., Boffi, J. C., Wang, L., Alhalaseh, K., Barbieri, M., Rehm, R., Deivasigamani, S., Gross, C. T., Agarwal, A., & Prevedel, R. (2021). High-resolution structural and functional deep brain imaging using adaptive optics three-photon microscopy. *Nature Methods*, *18*(10), 1253–1258. https://doi.org/10.1038/s41592-021-01257-6

Sul, J. H., Kim, H., Huh, N., Lee, D., & Jung, M. W. (2010). Distinct Roles of Rodent Orbitofrontal and Medial Prefrontal Cortex in Decision Making. *Neuron*, *66*(3), 449–460. https://doi.org/10.1016/j.neuron.2010.03.033

Takasaki, K., Larkin, J., Abbasi-Asl, R., Denman, D., Millman, D., de Vries, S., Takeno, M., da Costa, N. M., Reid, R. C., & Waters, J. (2019). 3-Photon Calcium Imaging of Deep Cortical Layers for Functional Connectomics. *Biophotonics Congress: Optics in the*

Life Sciences Congress 2019 (BODA,BRAIN,NTM,OMA,OMP), BM4A.4. https://doi.org/10.1364/BRAIN.2019.BM4A.4

Turaga, D., & Holy, T. E. (2010). Image-based calibration of a deformable mirror in wide-field microscopy. *Applied Optics*, *49*(11), 2030–2040. https://doi.org/10.1364/AO.49.002030

Wahl, D. J., Zhang, P., Mocci, J., Quintavalla, M., Muradore, R., Jian, Y., Bonora, S., Sarunic, M. V., & Zawadzki, R. J. (2019). Adaptive optics in the mouse eye: Wavefront sensing based vs. Image-guided aberration correction. *Biomedical Optics Express*, *10*(9), 4757–4774. https://doi.org/10.1364/BOE.10.004757

Wang, T., & Xu, C. (2020). Three-photon neuronal imaging in deep mouse brain. *Optica*, *7*(8), 947–960. https://doi.org/10.1364/OPTICA.395825

Xiao, Y., Deng, P., Zhao, Y., Yang, S., & Li, B. (2023). Three-photon excited fluorescence imaging in neuroscience: From principles to applications. *Frontiers in Neuroscience*, *Volume 17-2023*. https://www.frontiersin.org/journals/neuroscience/articles/10.3389/fnins.2023.1085682

Xiaodong Tao, Ju Lu, Tuwin Lam, Ramiro Rodriguez, Yi Zuo, & Joel Kubby. (2017). *A three-photon microscope with adaptive optics for deep-tissue in vivo structural and functional brain imaging*. *10051*, 100510R. https://doi.org/10.1117/12.2253922

Zeeb, F. D., Baarendse, P. J. J., Vanderschuren, L. J. M. J., & Winstanley, C. A. (2015). Inactivation of the prelimbic or infralimbic cortex impairs decision-making in the rat gambling task. *Psychopharmacology*, *232*(24), 4481–4491. https://doi.org/10.1007/s00213-015-4075-y

Zernike, von F. (1934). Beugungstheorie des schneidenver-fahrens und seiner verbesserten form, der phasenkontrastmethode. *Physica*, *1*(7), 689–704. https://doi.org/10.1016/S0031-8914(34)80259-5

Zhang, Q., Hu, Q., Berlage, C., Kner, P., Judkewitz, B., Booth, M., & Ji, N. (2023). Adaptive optics for optical microscopy [Invited]. *Biomedical Optics Express*, *14*(4), 1732–1756.

https://doi.org/10.1364/BOE.479886